Materials Advances

COMMUNICATION

Check for updates

Utilization of neural network potential for determining perovskite-type metal oxide photocathodes capable of producing hydrogen†

Shuya Masuda, [ID] [ab] Yosuke Harashima, [ID] [a] Tomoaki Takayama, [ID] *[a] Shogo Takasuka [ID] [a] and Mikiya Fujii [ID] *[a]

Metal−oxide-based photoelectrodes are promising candidates for water splitting because of their stability, but there is a lack of metal−oxide-based photocathodes. We proposed a method for determining such photocathodes by utilizing neural network potential, leading to the experimental discovery of a new PrCrO₃ photocathode capable of photoelectrochemically producing hydrogen in aqueous solution.

Photoelectrochemical cells are promising candidates for fabricating useful devices to generate hydrogen by splitting water using photon energy.[1–4] Such cells consist of a photocathode and a photoanode. Photocathodes play a role in hydrogen production and must possess a p-type semiconductor property. In contrast, photoanodes play a role in oxygen production, and their semiconductor property shall be n-type. As candidate materials for photocathodes and photoanodes, metal oxides are preferred to other inorganic materials such as metal sulfides because of their ease of synthesis and stability under water-splitting conditions.[5] However, most metal oxide semiconductors exhibit n-type properties originating from the easy formation of oxygen defects during their synthesis.[6,7] This situation makes experimentally discovering p-type metal oxide semiconductors challenging. To solve this problem, it is essential to establish a methodology to determine the likelihood that a metal oxide is p-type *in silico*. This methodology will facilitate the experimental discovery of new p-type metal oxide semiconductors, accelerating the progress in photoelectrochemical water splitting.

Density functional theory (DFT) calculations have been frequently used to distinguish the semiconductor properties of metal oxides.[8–11] These DFT-based methods can predict the p-type and n-type nature with high accuracy, and the explanations based on electronic states are understandable. However, in order to facilitate experimental discovery of p-type semiconductor materials, it is desirable to establish another methodology involved with more experimentally understandable insights, such as the equilibrium theory. In terms of facilitation, the fact that the DFT-based methods using hybrid functionals are quite time-consuming is another concern.

In the context of the aforementioned factors, interdisciplinary studies of materials science and information science have gathered increasing attention for efficiently designing inorganic materials, such as photocatalysts for water-splitting.[12,13] Herein, we combined insights from defect chemistry in materials science with the computational efficiency of neural network potential (NNP) to determine the likelihood that a metal oxide is p-type *in silico*. According to defect chemistry, comparison of the formation energies of the defects in crystal structures sheds light on the potential of metal oxides to become p-type. Specifically, the predominant formation of vacancy defects at the sites of metal cations, V_M, results in a p-type semiconductor property,[14] whereas the formation of vacancy defects at the sites of oxygen anions, V_O, results in an n-type semiconductor property.[15] Therefore, it is vital to estimate the formation energy of defects for discriminating the p-type semiconductor properties of metal oxides from the n-type ones with high-throughput computation. However, conventional DFT calculations for the exhaustive estimation of defect energies frequently suffer from time-consuming procedures. To advance this situation of computational material designs, we focused on NNP, which is expected to be an alternative high-throughput computational technique to DFT calculations.[16–18] NNP is a machine learning method that predicts interatomic potentials. The use of interatomic potentials allows faster structure optimization by calculating atomic forces from energy derivatives with respect to atomic coordinates. Recently, NNP has been applied to designing inorganic materials, for example in catalysis,[19,20]

[a] Graduate School of Science and Technology, Division of Materials Science, Nara Institute of Science and Technology, Nara 630-0192, Japan

[b] Digital Transformation Laboratory, Sumitomo Electric Industries Ltd., Osaka 554-0024, Japan. E-mail: takayama.tomoaki@ms.naist.jp, fujii.mikiya@ms.naist.jp

† Electronic supplementary information (ESI) available. See DOI: https://doi.org/10.1039/d5ma00220f

batteries,[21,22] glasses,[23] and semiconductors.[24] In defect chemistry, NNP has been used to study various defects, including vacancies,[25] dopants,[26] complex defects,[27] and surface defects.[28]

In this study, we report the effectiveness of NNP for extracting a new photocathode from a metal oxide database. First, we extracted 65 crystal structures of perovskite-type metal oxides from the Materials Project database.[29] Second, we labeled information on the semiconductor properties (*i.e.*, p- or n-type) of the 65 extracted compounds gathered from 38 references. The criteria for data extraction and the references collected are described in the ESI.† Hereafter, the gathered information is called "Label". Then, we calculated the formation energies of the defects of the metal cations and oxygen anions in the metal oxides using NNP. In addition, a subset of the metal oxides underwent DFT calculations to ascertain the reliability of NNP. Subsequently, we investigated the relationship between the calculated defect energies using NNP and their label (p-type or n-type). Consequently, it was determined that the formation energy of defects provides a readily comprehensible indicator from the perspective of physical chemistry, facilitating the classification of semiconductor characteristics. Finally, we experimentally discovered a new metal oxide photocathode in accordance with the classifier based on the investigated relationship.

Prior to the application of NNP for the estimation of the formation energies of the defects of the metal cations and oxygen anions in the 65 metal oxides (see the ESI,† for the details), the deviation of NNP from the DFT was evaluated. Matlantis[30,31] was used for NNP calculations, and VASP[32] was used for DFT calculations. The detailed calculation conditions are described in the ESI.† We focused on the differences in the energies between the perfect crystal structures and the corresponding defect-containing structures obtained by NNP and DFT. The energies exhibited a tendency to be proportional, as evidenced by the determination coefficient of 0.95 (see Fig. S1, ESI†). It is noteworthy that the training data for NNP in Matlantis does not include complex metal oxides, such as perovskite structures.[30] This is most likely because the training data of NNP include many types of polyhedral units that can be regarded as the building blocks of perovskites containing metal cations and oxygen anions. Therefore, it could be concluded that NNP can be used as an alternative to DFT for estimating the formation energies of defects. A comparison of NNP with other functionals of DFT is summarized in Fig. S2 (ESI†).

The relationship between the formation energies of the defects estimated by NNP in the 65 extracted metal oxides and their Labels were evaluated as shown in Fig. 1 and Table 1. Note that we estimated the formation energies of the defects according to eqn (S1), given in the ESI.† Before discussing the evaluation, brief interpretations of Fig. 1 and Table 1 are provided. Referring to the classification criterion defined above, the predominant defect formation in metal cations results in a p-type semiconductor property,[14] whereas an increase in defect formation in oxygen anions results in an n-type semiconductor property.[15] Therefore, as shown in Fig. 1, if a metal oxide is plotted in the red-filled region, the metal oxide
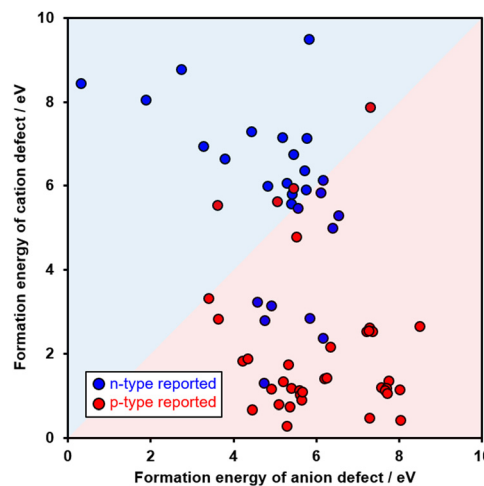

Fig. 1 The classification of the Labels (p- and n-types) on the basis of the formation energies of the cation and anion defects. These energies of the 65 extracted metal oxides were estimated using NNP. The red and blue circles indicate the compositions experimentally reported as p-type and n-type, respectively. In an ideal situation, red circles (blue circles) present in the blue-filled (red-filled) region would be located in the red-filled (blue-filled) region.

Table 1 Summary of the classification results

		Classified data		
		p-type	n-type	
Real data	p-type	33	4	Recall 89%
	n-type	12	16	Recall 57%
		Precision 73%	Precision 80%	Accuracy 75%

is classified as p-type. For classification as n-type, its plot is located within the blue-filled region. Blue circles indicate n-type Labels, and red circles indicate p-type Labels. Ideally, the red circles would only be located in the red-filled region, and the blue circles would be located in the blue-filled region. In addition, the accuracy, precision, and recall metrics of the typical assessment criteria in informatics are summarized in Table 1. The evaluations of Fig. 1 and Table 1 are summarized as follows. The accuracy of the overall classification of both Labels was 75%. For the p-type, precision and recall were 73% and 89%, respectively. This high recall value indicates that the proposed method can efficiently classify p-type oxides. Alternatively, for the n-type, precision and recall were 80% and 57%, respectively. The reason why the recall of the n-type was moderate would be the deviation of the calculation conditions of NNP from experimental conditions. Oxygen defects become more favorable at higher temperatures owing to the endothermic process to release the O_2 molecules into the gas phase from the crystal structures. Therefore, a material computationally (namely, at 0 K) classified as p-type could exhibit n-type behavior experimentally because of experimental preparation

at high temperature. In this section, it can be concluded that the relationship between the formation energies of the defects is a potent classifier for determining the likelihood that a metal oxide is p-type *in silico*.

We examined the effectiveness of the classifier for experimentally determining photocathodes. This is because metal oxides possessing p-type semiconductor properties could be applied as photocathodes. Among the 65 metal oxides shown in Fig. 1, 12 metal oxides were selected for the examination from the standpoint of their experimental synthesizability in the adopted solid-state reaction. The detailed solid-state reaction conditions are described in the ESI.† Among the selected 12 metal oxides, 3 metal oxides ($CaSnO_3$, $SrSnO_3$, and $SrTiO_3$) had been reported as n-type, whereas the other 9 metal oxides had been reported as p-type. Their photoelectrochemical properties were measured using a typical three-electrode-type cell in an aqueous K_2SO_4 electrolyte containing phosphate buffer (pH7) saturated with O_2. This O_2 gas was used as an electron scavenger to easily observe the cathodic photoresponse.

Fig. 2 shows the experimental validation of the likelihood that the selected metal oxides are p-type. In an ideal situation, the nine metal oxides plotted within or near the red area show not anodic but cathodic photoresponses. Firstly, by focusing on the nine metal oxides plotted within or near the red area, two metal oxides ($LaCrO_3$ and $PrCrO_3$; their X-ray diffraction patterns are shown in Fig. S3, ESI†) exhibited cathodic photoresponses under ultraviolet (UV) light irradiation, as shown by the red-filled circles. Contrary to the expectations, the other seven metal oxides exhibited anodic photoresponses (red-lined circles). Secondly, $CaSnO_3$, $SrSnO_3$, and $SrTiO_3$ classified as n-type predictably yielded anodic photoresponses (blue-filled circles). The discrepancy between the classification and the experimental results, as represented by the red-lined circles, can be explained as follows. From the standpoint of experiments on metal oxides, the higher the calcination temperature the easier the release of oxygen from the metal oxides. Taking $SrFeO_3$ as an example, it is observed that if the calcination temperature exceeds 400 °C, the number of oxygen defects increases.[33] In addition, metal oxides with high oxygen deficiency are generally n-type.[15] For our experiments, we used high-temperature calcination (1150 °C) for solid-state reactions in air because of the simplicity of synthesis. This calcination temperature was higher than the synthesis temperatures (*e.g.*, 200 °C) reported in the literature that we collected (38 papers listed in the ESI†). Therefore, our experimental conditions were concluded to be prone to generating the defects of oxygen anions as compared to those of the collected literature from the viewpoint of the experimentally thermodynamic equilibrium. Nevertheless, $LaCrO_3$ and $PrCrO_3$ exhibited photocathodic properties. This is owing to the durability of oxygen anions against defect formation, as suggested from Fig. 2. Specifically, the formation energies of the anion defect in $LaCrO_3$ and $PrCrO_3$ were the two highest energies among the 12 compositions that we synthesized. Importantly, to the best of our knowledge, there is no report suggesting that $PrCrO_3$ provides a cathodic photoresponse. Thus, it could be concluded that the relationship between the formation energies of the defects of the metal cations and oxygen anions estimated by NNP is a potent guideline for determining the likelihood that a metal oxide is a photocathode *in silico*.

$PrCrO_3$ photocathode further underwent a photoelectrochemical hydrogen production reaction. $PrCrO_3$ thin film (its X-ray diffraction pattern is shown in Fig. S4, ESI†) was additionally prepared using a spin-coat method (see the ESI,† for details) instead of a solid-state reaction considering the generally superior experimental performances of the thin-film photocathodes to particulate-based photocathodes. Cross-sectional scanning electron microscopy (SEM) was conducted using a $PrCrO_3$ photocathode (Fig. S5, ESI†). The FTO substrate was covered with a thin film. The thickness was approximately 100 nm. SEM with energy-dispersive X-ray spectroscopy (SEM-EDX) was additionally conducted (Fig. S6, ESI†). Elemental maps of Pr, Cr, and O were clearly recorded in addition to Si and Sn. The overlay of these maps indicated that the observed thin film was composed of Pr, Cr, and O. Fig. 3 shows the linear sweep voltammogram of the $PrCrO_3$ thin film photocathode. An aqueous electrolyte comprising phosphate buffer (pH7) saturated with Ar instead of O_2 was used. Cathodic photocurrent was clearly observed when the $PrCrO_3$ thin film photocathode was irradiated with UV light (namely, "light on" in the inset of Fig. 3). In contrast, such a cathodic photocurrent immediately disappeared under dark (namely, "light off" in the inset of Fig. 3). The details of the voltammogram are shown in Fig. S7 (ESI†). Mott–Schottky analysis indicated that the flat-band potential of a $PrCrO_3$ photocathode was about +0.7 V *vs.* RHE (Fig. S8, ESI†). This flat-band potential was relatively more positive, for example, than that of Cu_2O (*e.g.*, +0.55 V *vs.* RHE).[34] The positive flat-band potential is desirable for the
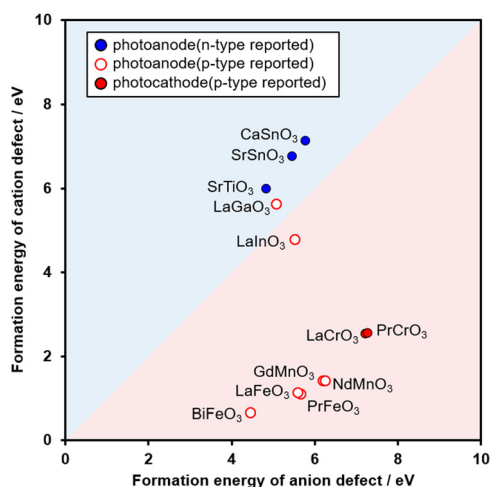

Fig. 2 Photoelectrochemical measurement results for metal oxides synthesized through the solid-state reaction. The blue-filled (red-filled) circles indicate that their observed photoanodic (photocathodic) properties were consistent with their n-type (p-type) semiconductor properties experimentally recorded in the literature. In contrast, the red-lined circles indicate the inconsistency between their observed photoanodic properties and their p-type semiconductor properties recorded in the literature.
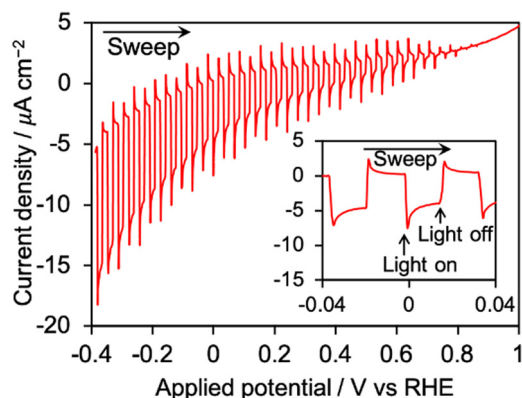
Fig. 3 Linear sweep voltammogram of the PrCrO$_3$ thin film photocathode. The inset figure is the magnified image of the area around 0 V vs. RHE. Light source: a 300 W Xe-arc lamp (λ > 300 nm), electrolyte: an aqueous K$_2$SO$_4$ solution containing phosphate buffer (pH7) saturated with Ar, electrode area: approximately 1 cm^2.

construction of a photoelectrochemical cell, as discussed in the latter section. According to Mott–Schottky plots, the carrier concentration of the PrCrO$_3$ photocathode was estimated to range from 1.1×10^{14} to 3.2×10^{15} cm^{-3}, when the dielectric constant of PrCrO$_3$ was assumed to be the same as that reported in the literature (from 1000 to 30 000 F m^{-1}).[35,36]

Fig. 4 shows the dependence of the cathodic photocurrent on the cut-off wavelengths of the irradiation light. The time-course of the wavelength-dependencies is provided in Fig. S9 (ESI†). The onset of the photocurrent was near ~400 nm of the cut-off wavelength. Such an onset indicated that the observed photocurrents were obtained by the band gap excitation of PrCrO$_3$ rather than the d–d transition of Cr ions, attributed to the absorption of visible light.[37] Fig. 5 shows photoelectrochemical hydrogen production using the PrCrO$_3$ thin film photocathode under UV light irradiation. The applied potential was 0 V vs. RHE. Its cathodic photocurrent was recorded for 120 min under UV light irradiation, whereas the photocurrent was negligible in the dark again. Most importantly, H$_2$ was
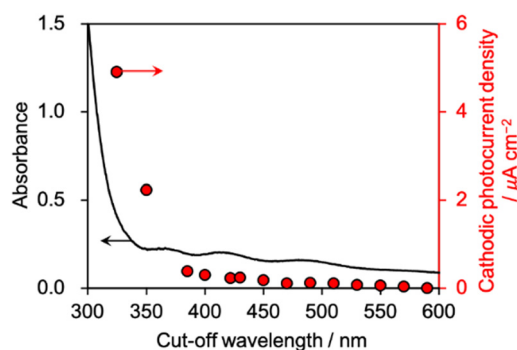

Fig. 4 Dependence of the cathodic photocurrent density of the PrCrO$_3$ thin film photocathode on the cut-off wavelength of the incident light. Light source: a 300 W Xe-arc lamp equipped with the corresponding cut-off filters (namely, slong pass filters), electrolyte: an aqueous K$_2$SO$_4$ solution containing phthalate buffer (pH4) saturated with Ar, applied potential: −0.4 V vs. RHE, electrode area: approximately 1 cm^2.
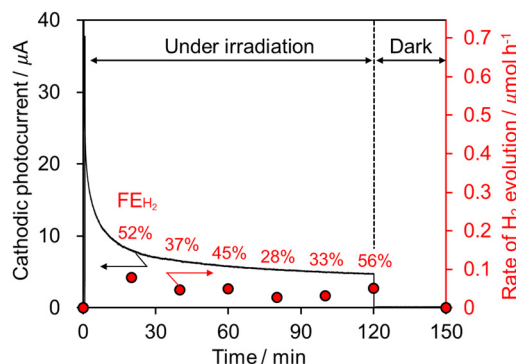

Fig. 5 Photoelectrochemical H$_2$ production using the PrCrO$_3$ thin film photocathode under UV irradiation. Light source: a 300 W Xe-arc lamp (λ > 300 nm), electrolyte: an aqueous K$_2$SO$_4$ solution containing phosphate buffer (pH7) saturated with Ar, applied potential: 0 V vs. RHE, electrode area: approximately 6 cm^2.

continuously detected during UV light irradiation, whereas H$_2$ was not detected in the dark. These results indicated that the observed cathodic photocurrent was consumed for H$_2$ production at 0 V vs. RHE in an aqueous neutral electrolyte. The faradaic efficiency for H$_2$ production (FE$_{H_2}$) on the PrCrO$_3$ photocathode was estimated at each sampling points, resulting in an averaged faradaic efficiency of 42%. The reason why the FE$_{H_2}$ was below 100% is most likely due to the small amount of H$_2$ gas being close to the limit of quantification. It is noteworthy that a tandem cell consisting of a PrCrO$_3$ photocathode and a CoO$_x$/BiVO$_4$:Mo photoanode gave photocurrents under simulated sunlight irradiation without an external electronic voltage (Fig. S10, ESI†). This is because of the clear overlap between the onsets of the photocurrents of the PrCrO$_3$ photocathode and CoO$_x$/BiVO$_4$:Mo photoanode (Fig. S11, ESI†). Thus, we successfully demonstrated that PrCrO$_3$ is a new photocathode capable of producing H$_2$ utilizing UV light in accordance with the classification. Although PrCrO$_3$ primarily responds to ultraviolet light, its performance could be improved by doping to increase carrier concentration and enhance visible light absorption. Our findings based on NNP are expected to be beneficial for the assessment of doped structures.

Conclusions

We established a method combining the insights of defect chemistry with the computational efficiency of NNP to extract metal oxide photocathodes with perovskite-type crystal structures from the Materials Project database of inorganic materials. The deviation of the formation energies of the defects of metal cations and oxygen anions estimated by NNP from those estimated by DFT is fairly small in the representatives of the extracted metal oxides, indicating the reliance of NNP in the estimations instead of DFT. The estimation of the formation energies of the defects using NNP is effective in classifying their semiconductor properties into p- or n-type. The accuracy of the proposed classification method for the p-type and n-type Labels

obtained by reference was 75%. The accuracy would be improved through the incorporation of finite-temperature effects into NNP-based estimations. According to this classification, we experimentally discovered a new $PrCrO_3$ photocathode capable of photoelectrochemically producing H_2 utilizing UV light. This finding will accelerate the discovery of new metal oxide photocathodes for photoelectrochemical H_2 production.

Author contributions

Shuya Masuda: data curation, formal analysis, investigation, validation, visualization, and writing – original draft. Yosuke Harashima: conceptualization and writing–review & editing. Tomoaki Takayama: supervision, conceptualization, project administration, and writing – review & editing. Shogo Takasuka: supervision and writing – review & editing. Mikiya Fujii: supervision and writing – review & editing.

Conflicts of interest

There are no conflicts to declare.

Data availability

The data supporting this article have been included as part of the ESI.†

Acknowledgements

Notes and references

1 A. Kudo and Y. Miseki, *Chem. Soc. Rev.*, 2009, **38**, 253.
2 R. Abe, *J. Photochem. Photobiol.*, 2010, **11**, 179.
3 F. E. Osterloh, *Chem. Soc. Rev.*, 2013, **42**, 2294.
4 T. Hisatomi, J. Kubota and K. Domen, *Chem. Soc. Rev.*, 2014, **43**, 7520.
5 Y. Chen, X. Feng, Y. Liu, X. Guan, C. Burda and L. Guo, *ACS Energy Lett.*, 2020, **5**, 844.
6 J. Robertson and Z. Zhang, *MRS Bull.*, 2021, **46**, 1037.
7 A. Samizo, M. Minohara, N. Kikuchi, K. Bando, Y. Aiura, K. Mibu and K. Nishio, *J. Phys. Chem. C*, 2021, **125**, 17117.
8 W. Li, C. F. J. Walther, A. Kuc and T. Heine, *J. Chem. Theory Comput.*, 2013, **9**, 2950.
9 G. Hautier, A. Miglio, D. Waroquiers, G. M. Rignanese and X. Gonze, *Chem. Mater.*, 2014, **26**, 5447.
10 N. Sarmadian, R. Saniz, B. Partoens and D. Lamoen, *Sci. Rep.*, 2016, **6**, 20446.
11 K. Yim, Y. Youn, M. Lee, D. Yoo, J. Lee, S. H. Cho and S. Han, *Npj Comput. Mater.*, 2018, **4**, 17.
12 P. O. Dral, *Chem. Commun.*, 2024, **60**, 3240.
13 D. Chen, C. Shang and Z. P. Liu, *Npj Comput. Mater.*, 2023, **9**, 2.
14 M. Nolan and S. D. Elliott, *Phys. Chem. Chem. Phys.*, 2006, **8**, 5350.
15 M. E. Seyed, R. E. Mohammad, B. A. Reza and K. Hadi, *Phys. Chem. Res.*, 2018, **6**, 547.
16 S. Käser, L. I. Vazquez-Salazar, M. Meuwly and K. Töpfer, *Digital Discovery*, 2023, **2**, 28.
17 J. S. Smith, O. Isayev and A. E. Roitberg, *Science*, 2017, **8**, 3192.
18 T. Xie and J. C. Grossman, *Phys. Rev. Lett.*, 2018, **120**, 145301.
19 T. Kobayashi, D. J. Liu and F. A. Perras, *Chem. Commun.*, 2022, **58**, 13939.
20 T. Koyama, M. Nakayama and J. Schuett, *J. Phys. Chem. C*, 2024, **128**, 19482.
21 R. Iwasaki, N. Tanibata, H. Takeda and M. Nakayama, *Commun. Mater.*, 2024, **5**, 148.
22 W. Wang, T. Yang, W. H. Harris and R. Gómez-Bombarelli, *Chem. Commun.*, 2020, **56**, 8920.
23 R. Kayano, Y. Inagaki, R. Matsubara, K. Ishida and T. Ohkubo, *J. Phys. Chem. C*, 2023, **128**, 17686.
24 C. Hong, S. Oh, H. An, P. H. Kim, Y. Kim, J. H. Ko, J. Sue, D. Oh, S. Park and S. Han, *ACS Appl. Mater. Interfaces*, 2024, **16**(36), 48457.
25 G. V. Huerta, K. Hisama, K. Sato, K. Nagaoka and M. Koyama, *iScience*, 2025, **28**, 112470.
26 T. Chen, E. H. Otal, T. Q. Nguyen, S. Narumi, M. Koyama and N. Zettsu, *Chem. Mater.*, 2025, **37**, 709.
27 J. Bae, C. Kwon, S.-O. Park, H. Jeong, T. Park, T. Jang, Y. Cho, S. Kim and S. Choi, *Sci. Adv.*, 2024, **10**, eadm7221.
28 B. G. Son, C. Kwon, Y. Cho, T. Jang, H. R. Byon, S. Kim and E. S. Cho, *ACS Appl. Mater. Interfaces*, 2024, **16**, 32259.
29 A. Jain, S. P. Ong, G. Hautier, W. Chen, W. D. Richards, S. Dacek, S. Cholia, D. Gunter, D. Skinner, G. Ceder and K. A. Persson, *APL Mater.*, 2013, **1**, 011002.
30 S. Takamoto, C. Shinagawa, D. Motoki, K. Nakago, W. Li, I. Kurata, T. Watanabe, Y. Yayama, H. Iriguchi, Y. Asano, T. Onodera, T. Ishii, T. Kudo, H. Ono, R. Sawada, R. Ishitani, M. Ong, T. Yamaguchi, T. Kataoka, A. Hayashi, N. Charoenphakdee and T. Ibuka, *Nat. Commun.*, 2022, **13**, 2991.
31 Matlantis, Preferred Computational Chemistry, Inc., https://matlantis.com/(accessed Jun 10, 2024).
32 G. Kresse and J. Furthmüller, *Phys. Rev. B: Condens. Matter Mater. Phys.*, 1996, **54**, 11169.
33 K. Shido, T. Yoshino, S. Hatano, M. Matsuo and T. Hashimoto, *Interactions*, 2024, **245**, 299.
34 D. Jeong, W. Jo, J. Jeong, T. Kim, S. Han, M.-K. Son and H. Jung, *RSC Adv.*, 2022, **12**, 2632.
35 R. Late, K. V. Wagaskar, P. B. Shelke and P. R. Sagdeo, *Mater. Chem. Phys.*, 2021, **252**, 124313.
36 B. V. Prasad, G. N. Rao, J. W. Chen and D. S. Babu, *Mater. Chem. Phys.*, 2011, **126**, 918.
37 R. Mguedla, A. B. J. Kharrat, O. Taktak, H. Souissi, S. Kammoun, K. Khirouni and W. Boujelben, *Opt. Mater.*, 2020, **101**, 109742.